Master Thesis

Thermodynamic Study on B and Fe Substituted $Cr_{23}C_6$ Using First-Principles Calculations

Song, You Young (宋侑映)

Computational Metallurgy

Graduate Institute of Ferrous Technology

Pohang University of Science and Technology

2010

Thermodynamic Study on B and Fe Substituted $Cr_{23}C_6$ Using First-Principles Calculations

2010 Song, You Young

제일원리를 이용한 $Cr_{23}C_6$ 열역학 계산

Thermodynamic Study on B and Fe Substituted $Cr_{23}C_6$ Using First-Principles Calculations

Thermodynamic Study on B and Fe Substituted $Cr_{23}C_6$ Using First-Principles Calculations

by

Song, You Young
Department of Ferrous Technology
(Computational Metallurgy)
Graduate Institute of Ferrous Technology
Pohang University of Science and Technology

A thesis submitted to the faculty of Pohang University of Science and Technology in partial fulfillments of the requirements for the degree of Master of Science in the Graduate Institute of Ferrous Technology (Computational Metallurgy)

Pohang, Korea
April 15th, 2010

Approved by

Prof. Bhadeshia, H. K. D. H.	Prof. Kim, In Gee
H. D. Bhadeshia	
Major Advisor	Co-Advisor

Thermodynamic Study on B and Fe Substituted $Cr_{23}C_6$ Using First-Principles Calculations

Song, You Young

This dissertation is submitted for the degree of Master of Science at the Graduate Institute of Ferrous Technology of Pohang University of Science and Technology. The research reported herein was approved by the committee of Thesis Appraisal

April 15th, 2010

Thesis Review Committee

Chairman: Prof. Bhadeshia, H. K. D. H.
(signature) H. D. Bhadeshia

Member: Prof. Kim, In Gee
(signature)

Member: Prof. Suh, Dong-Woo
(signature)

Preface

This dissertion is submitted for the degree of Master of Engineering in Computational Metallurgy at Pohang University of Science and Technology. The research described herein was conducted under the supervision of Professor H. K. D. H. Bhadeshia, Professor of Computational Metallurgy in the Graduate Institute of Ferrous Technology, Pohang University of Science and Technology and Tata Steel Professor of Metallurgy, University of Cambridge, and Professor In Gee Kim, Professor of Computational Metallurgy between September 2008 and June 2010.

Except where acknowledgement and reference is made to previous work, this work is, to the best of my knowledge, original. Neither this, nor any substantially similar dissertation has been, or is being, submitted for any other degree, diploma or other qualification at any other university.

Part of this work will be submitted to appear in the publication in the future.

Song, You Young

June 2010

Acknowledgement

I am deeply grateful to my supervisor, Professor In Gee Kim for his constant guidance and support. I am thankful to Professor Bhadeshia, H. K. D. H. for his guidance and friendship as my supervisor. I also want to express my great thanks to Professor Dong-Woo Suh and Professor Hae-Geon Lee for their advice and support.

I would like to express my thanks to all the people in the Graduate Institute of Ferrous Technology (GIFT) in Pohang University of Science and Technology, especially those members in Computational Metallurgy Laboratory (CML), for all their help and for all the memories we have. The life with CML members was quite pleasant and enjoyable.

I would like to thank to Professor Auther Freeman and the group members for help and friendship during my stay in Northwestern University.

Finally, I would like to take this opportunity to express my gratitude to my family and Min Sung Joo for their love, unfailing encouragement and support.

Song, You Young

June 2010

MFT Song, You Young
20081010 Thermodynamic Study on B and Fe Substituted $Cr_{23}C_6$ Using First-principles Calculations,
Department of Ferrous Technology
(Computational Metallugy) 2010
Advisor: Bhadeshia, H. K. D. H.; Prof. Kim, In Gee
Text in English

Abstract

$Cr_{23}C_6$ and its various solid solutions are vital phases in the most modern of creep-resistant steels. Boron is known to increase the creep resistance by stabilizing $M_{23}C_6$ carbides, but although there has been a great deal of work in understanding its significance with respect to elevated temperature properties, the detailed thermodynamic properties deserve further attention. The standard thermodynamic assessments which are based on macroscopic measurements do not reveal such information. To work towards this goal, we use the all-electron full potential linearized augmented plane-wave method (FLAPW) within the generalized gradient approximation. The formation enthalpy of $Cr_{23}C_6$ is calculated to be 1.82 kJ mol^{-1} higher than the lowest formation enthalpy of $FeCr_{22}C_6$. Dissolution of boron into $M_{23}C_6$ is calculated to stabilize the structure, having decreased formation enthalpy of -8.61 kJ mol^{-1}, -9.74 kJ mol^{-1} and -13.53 kJ mol^{-1} for $Cr_{23}C_6$, $Cr_{23}C_5B$ and $Cr_{23}B_6$, respectively. In future work we hope to incorporate the calculated energies into phase diagram calculation methods.

Contents

PREFACE I

ACKNOWLEDGEMENT II

ABSTRACT III

CONTENTS IV

NOMENCLATURE VI

I. INTRODUCTION 1

1.1. Power Plant Application 1

1.2. Creep-Resistant Steel 3
1.2.1. Creep Deformation 3
1.2.2. Creep-resistant Steels 6

1.3. Boron Effect on Creep 10

1.4. Boron and $M_{23}C_6$ Carbide 14
1.4.1. Carbides in Creep-resistant Steel 14
1.4.2. Boron and $M_{23}C_6$ 17

1.5. Previous Study on $M_{23}C_6$ 20
1.5.1. The Structural Properties of $Cr_{23}C_6$ 20
1.5.2. Thermodynamic Properties of $Cr_{23}C_6$ 23

II. FIRST-PRINCIPLES CALCULATION 25

2.1. Theoretical Background 26
2.1.1. Many-body Hamiltonian 27
2.1.2. Born-Oppenheimer Approximation 27
2.1.3. Many-electron System 28

2.2. Density Functional Theory 29
2.2.1. Hohenberg-Kohn Theorem 29
2.2.2. Kohn-Sham Equation 30
2.2.3. Exchange-Correlational Functional 31

2.3. The Full-Potential Linearized Augmented Plane-Wave (FLAPW) Method 33

2.4. Computational Method 35

III. RESULTS AND DISCUSSIONS 37

3.1. Lattice Parameter Optimization 38
3.1.1. Effect of Fe and B Substitution 41

3.2. The Formation Enthalpy 42

3.3. Bulk Moduli 46

3.4. Magnetic Properties 48

IV. CONCLUSIONS 49

REFERENCES 50

CURRICULUM VITAE 54

Nomenclature

3D-BZ	Three dimensional Brillouin zone
B	Bulk modulus
B'	The pressure derivative of bulk modulus
BCC	Body centered cubic
$Cr_{23}(C_5B)$	Structure with a carbon atom replaced by B at 24e
$Cr_{23}(C_{5-x}B_x)$	Structure with x carbon atoms replaced by x B atoms
DOS	Density of states
E_{GS}	The ground state energy
$E[n]$	Energy density functional
$E_{xc}[n]$	Exchange-correlation density functional
EOS	Equation of state
FCC	Faced centered cubic
$Fe^{4a}Cr_{22}C_6$	Structure with a chromium atom replaced by Fe at 4a
$Fe^{8c}Cr_{22}C_6$	Structure with a chromium atom replaced by Fe at 8c
$Fe^{32f}Cr_{22}C_6$	Structure with a chromium atom replaced by Fe at 32f
$Fe^{48h}Cr_{22}C_6$	Structure with a chromium atom replaced by Fe at 48h
FM	Ferromagnetic
H	Hamiltonian
GGA	Generalized gradient approximation
LDA	Local density approximation
MT	Muffin-tin

$n(\boldsymbol{r})$	Electronic density function
$n_{GS}(\boldsymbol{r})$	The ground state electronic density
NM	Nonmagnetic
PM	Paramagnetic
T_m	The absolute melting temperature
T_n	Nuclei kinetic part of Hamiltonian
T_e	Electronic kinetic part of Hamiltonian
ΔU	The formation energy
ΔH	The formation enthalpy
V_{n-n}	Interaction part between nuclei and nuclei
V_{e-e}	Interaction part between electrons and electrons
V_{n-e}	Interaction part between nuclei and electrons
V_{ext}	External potential
V_{eff}	Effective potential
Ψ	Wave function of Schrödinger equation
Ψ_{nuclei}	Wave function of nuclei part of Schrödinger equation
$\Psi_{\text{electrons}}$	Wave function of electronic part of Schrödinger equation

I. Introduction

Steel is the most prominent material used in industry and everyday life. It is because steel has the ability to satisfy a variety of requirements, often in severe environments, by processing and alloying control. Steels used in power plants are expected to maximize efficiency, minimize emission and have reliable service life while exposed to high temperatures and stresses for long periods. In power plant steels, creep strength is necessary along with corrosion and oxidation resistance as the temperatures involved can be as high as $650\,℃$. Carbide precipitates are known to influence the creep resistance; the most commonly observed carbide is $Cr_{23}C_6$ or chromium rich $M_{23}C_6$ where the 'M' indicates combinations of metal atoms. This thesis focuses on the thermodynamic and structural description of $M_{23}C_6$ with boron and iron solutes using first-principles.

1.1. Power Plant Application

Power plants produce electrical energy by running turbines connected to generators. Generators obtain thermal energy, which is in most cases steam, from fossil fuel combustion, then convert it into rotational energy and then into electricity. Thus, increasing the efficiency of a power plant depends on using less fuel and gaining more thermal energy for steam generation which is also important with respect to economic and environmental aspects.

The efficiency of steam power plants nowadays is around $42\,\%$ with a steam temperature of $600\,℃$ and pressure of $25-30$ MPa [Ennis, 2003]. Although

there are other control measures as shown in Table 1.1, increasing the steam temperature is necessary to achieve the thermal efficiency goal of 45 % or higher. Steels used in power plants are expected to help maximize energy efficiency, thus minimize CO_2 emissions and provide a reliable service life of about 30 years. However, creep limits the life with exposure to temperatures of 600 ℃. It is necessary therefore to develop better steel technologies to cope with this problem.

Control Measure	Increase in Efficiency / %
Reduction of condenser pressure by 50 %	1.5
60 ℃ increase in steam temperature	1.4
Use of double reheat	1
20 % increase in steam pressure	0.3
Reducing excess air by 10 %	0.25
10 ℃ decrease in flue gas temperature	0.25

Table 1.1 Anticipated efficiency improvements for changes in power plant operating conditions.
[Wachter and Ennis, 1995]

1.2. Creep-Resistant Steel

1.2.1. Creep Deformation

Creep is the time-independent permanent deformation of a material when exposed to astress. In metals, creep is important when the temperature is over approximately $0.4\,T_m$, where T_m is the absolute melting temperature. As the melting point of pure iron is known as $1811\,\mathrm{K}\,(1538\,℃)$, the steam temperature of $600\,℃$ is at the limits of this criterion.

In typical creep tests, a constant load is applied to the specimen which is maintained at constant temperature. A typical creep curve is shown in Figure 1.1 with the creep strain $\boldsymbol{\epsilon}$ measured as a function of elapsed time $\boldsymbol{t}$. In engineering situations the load is maintained constant. To understand the fundamental creep mechanism the stress is maintained constant.

A creep curve consists of three regions distinguished by the creep rate. The initial deformation is mostly elastic and appears as the load is applied to the specimen. The first part is called primary or transient creep where the creep rate continuously decreases by an increase in creep resistance or strain hardening as strained material is difficult to deform. This is followed by secondary or steady-state creep with the constant creep rate due to a balance between the competing processes of strain hardening and recovery. Tertiary creep is the last stage with an increasing creep rate until failure or rupture appears occurs in constant load creep tests at high stresses and temperatures. Rupture is related to microstructural or metallurgical changes such as coarsening of precipitates, grain boundary separation, *etc*.

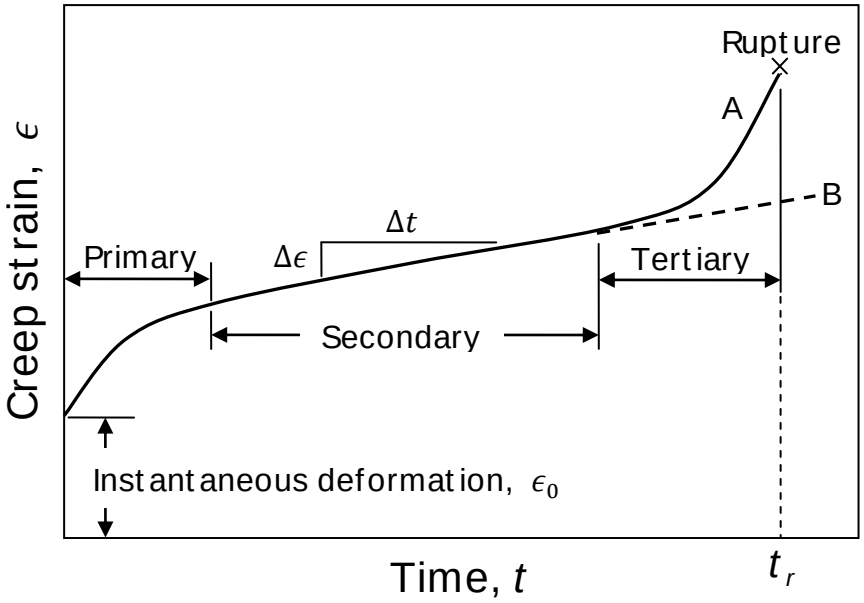

Figure 1.1 Typical creep curve of strain versus time at constant load A and constant stress B at constant elevated temperature. The minimum creep rate $\dot{\epsilon} = \Delta\epsilon/\Delta t$ is the slope of the linear segment in the secondary region. Rupture lifetime t_r is the total time to rupture.

Figure 1.2 shows the influence of stress and temperature on creep strain. Higher temperatures and stress increase the creep strain which will accelerate the creep rate and decrease the time to rupture. Increasing operating steam temperature and pressure to increase the thermal efficiency of the power plant would unacceptably shorten the lifetime of steels currently in service. Improved creep-resistant steels are required.

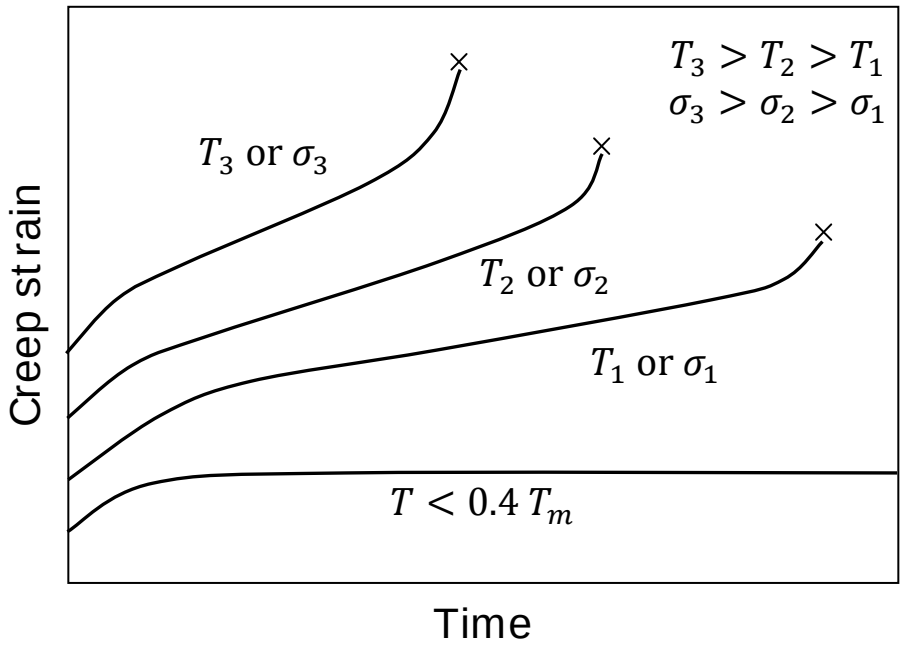

Figure 1.2 Influence of stress $\boldsymbol{\sigma}$ and temperature $\boldsymbol{T}$ on creep behavior. [Callister, 2007]

Power plant steel has a long service life which is about 30 years and failure can be dangerous – it is difficult to control the tertiary creep and the time to rupture is the initiation of that stage. Thus, the steady-state creep rate $\dot{\epsilon}$ is an important engineering design parameter for power plant components since decreased constant creep rate slows down the creep deformation and the total time to rupture increases. Through intensive experiments, alloying elements such as boron are known to decrease the secondary creep rate but the mechanism is not sufficiently understood.

1.2.2. Creep-resistant Steels

The development history of creep-resistant steels has led to high chromium steels with ferritic or martensitic microstructures.

Chromium is known to be a ferrite stabilizer and carbide former and up to 12 wt% of high chromium addition increases the hardenability and corrosion resistance. 9 – 12 wt% Cr steels with Mo added, were developed for steam turbine blades which need corrosion resistance. 12Cr steels having high temperature strength were then developed after the 1940s for jet engines. Now these high Cr steels are used in power plants.

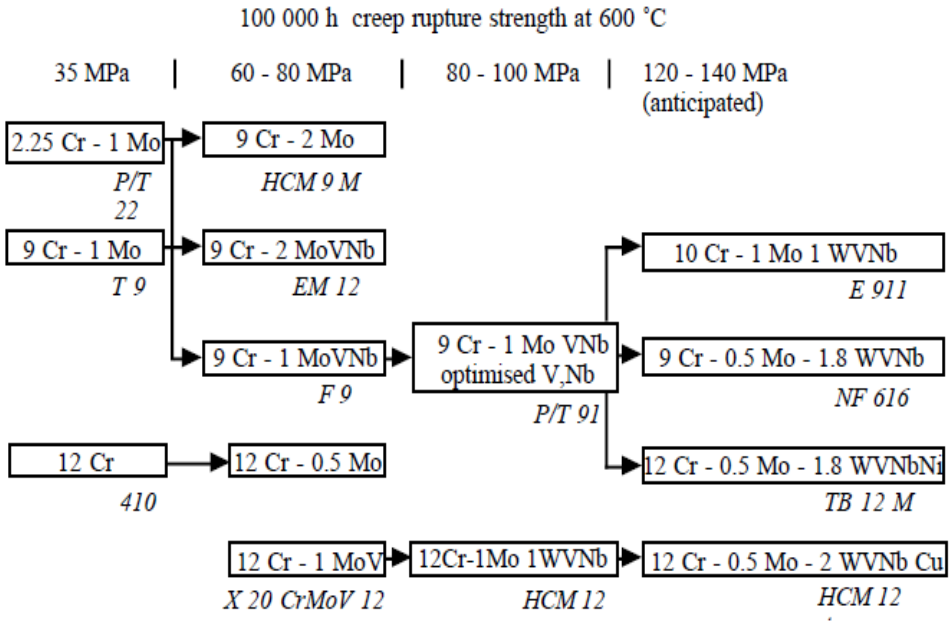

Figure 1.3 Flowchart of 9 to 12 wt% Cr Steels development. [Wachter and Ennis, 1995]

Figure 1.3 shows the flowchart of development of 9 to 12 wt% chromium steels. Additions of molybdenum, vanadium, tungsten, *etc*. into 9 - 12 wt% of Cr steels have increased the creep rupture strength at the temperature of 600 ℃ for 100,000 hours to about 100 MPa. The next generation of creep-resistant steels aims to achieve a minimum of 120 MPa of creep rupture strength at 600 ℃ or over. Table 1.2 shows the typical chemical compositions of creep-resistant steels. The most modern alloys are in the lower part of the table with higher chromium concentrations, to satisfy higher service temperatures.

Austenitic stainless steels were once thought to be promising materials for high temperature applications. The maximum operating temperature of currently used or newly developed power plant steels is compared based on 100000 h average stress rupture strength of 100 MPa is shown in Figure 1.4.

Austenitic stainless steels have reliable maximum operating temperatures which are over 600 ℃ and the 100000h creep rupture strength of austenitic stainless steel is higher than that of 9CrMoV and 12Cr1MoV steels [Blum *et al*., 1993]. The cost of austenitic stainless steels is high because of high chromium and nickel concentrations than 9 to 12 wt% Cr creep-resistant steels that also have operating temperature over 600 ℃ in Figure 1.4 but however, this is not the only reason that they are not used for power plant applications. The thermal expansion coefficient of austenitic steel is 50 % higher and the thermal conductivity is 50 % lower than ferritic steels as listed in Table 1.3 for example. Thermal fatigue can happen during cooling and heating in this case and that will eventually restrict the lifetime which is

not appealing to use austenitic steels. Thus 9 – 12 wt% ferritic and martensitic steels are being developed for in use of power plant or high temperature applications.

Designation	C	Si	Mn	Ni	Mo	Cr	V
1Cr$\frac{1}{2}$Mo	0.15	0.25	0.50	–	0.6	0.95	
$\frac{1}{4}$CrMoV	0.15	0.25	0.50	0.05	0.50	0.30	0.25
$\frac{1}{2}$Cr$\frac{1}{2}$Mo$\frac{1}{4}$V	0.12	0.25	0.50	–	0.6	0.45	0.25
1CrMoV	0.25	0.25	0.75	0.70	1.00	1.10	0.35
2$\frac{1}{4}$Cr1Mo	0.15	0.25	0.50	0.10	1.00	2.30	0.00
Mod. 2$\frac{1}{4}$Cr1Mo	0.1	0.05	0.5	0.16	1.00	2.30	0.25
						Ti=0.03	B=0.0024
2$\frac{1}{4}$Cr1.6WV	0.05	0.20	0.50	–	0.10	2.20	0.20
						W=1.60	Nb=0.05
3.0Cr1.5Mo	0.1	0.2	1.0	0.1	1.5	3.0	0.1
3.5NiCrMoV	0.24	0.01	0.20	3.50	0.45	1.70	0.10
9Cr1Mo	0.10	0.60	0.40	–	1.00	9.00	–
Mod. 9Cr1Mo	0.1	0.35	0.40	0.05	0.95	8.75	0.22
					Nb=0.08	N=0.05	Al <0.04
9Cr$\frac{1}{2}$MoWV	0.11	0.04	0.45	0.05	0.50	9.00	0.20
					W=1.84	Nb=0.07	N=0.05
12CrMoV	0.20	0.25	0.50	0.50	1.00	11.25	0.30
12CrMoVW	0.20	0.25	0.50	0.50	1.00	11.25	0.30
							W=0.35
12CrMoVNb	0.15	0.20	0.80	0.75	0.55	11.50	0.28
						Nb 0.30	N 0.06

Table 1.2 Typical compositions (wt %) of creep-resistant steels. [Bhadeshia, 2001]

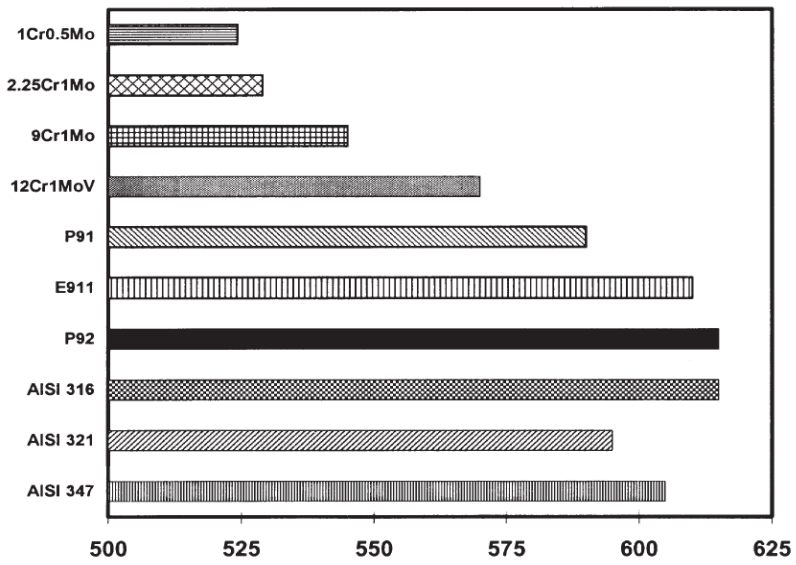

Figure 1.4 Maximum operating temperature (℃), based on a 100000h average stress rupture strength of 100 MPa

[Ennis *et al.*, 2003]

Steel	Thermal expansion coefficient / W m^{-1} K^{-1}	Thermal conductivity / μ K^{-1}
12Cr ferritic	9.9	24.9
20CrNi austenitic	15.3	13.5

Table 1.3 Thermal expansion coefficient and thermal conductivity of an austenitic and a ferritic stainless steel [Harvey, 1982].

1.3. Boron Effect on Creep

A small amount of boron is known to remarkably increase the hardenability of steel. Boron added steel is attractive to industry as expensive alloying elements such as molybdenum can be substituted by boron and will maintain high temperature strength. However, since excessive boron additions cause embrittlement due to the formation of compounds, it is important to know its optimum concentration.

Some experimental studies reported that boron additions increase creep rupture strength [Mimino, 1978] and decrease the creep rate [Hofer *et al*., 2002; Albert *et al*., 2005; Horiuchi *et al*., 2002].

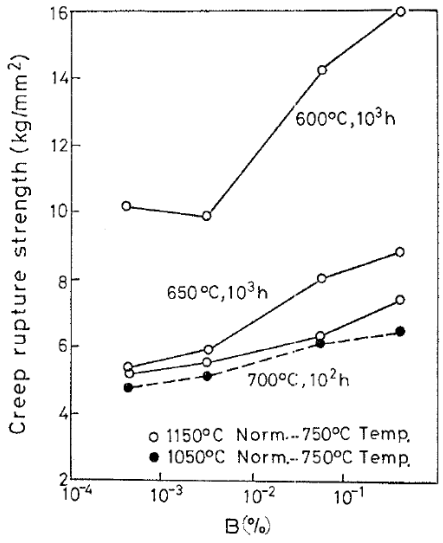

Figure 1.5 Change of creep-rupture strength of 9Cr-1Mo-V-Nb with addition of B.
[Mimino, 1978]

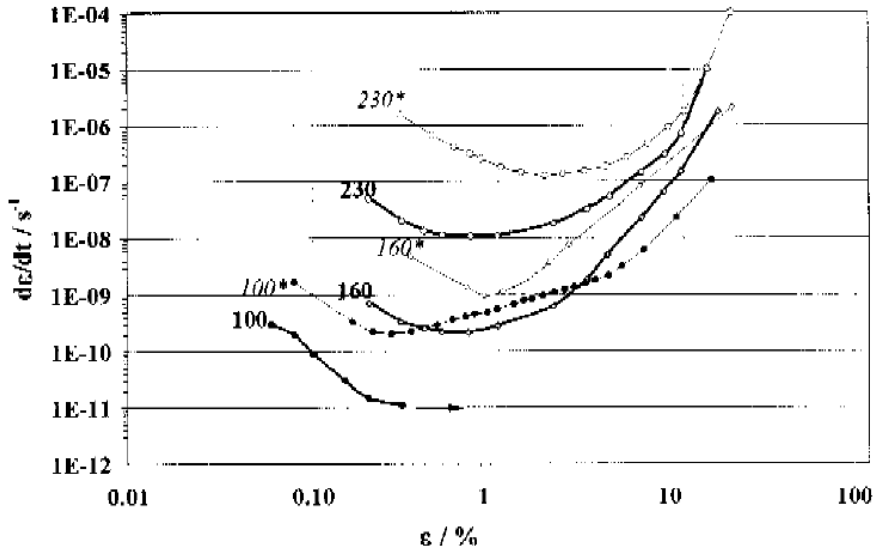

Figure 1.6 Creep rate for different stresses (MPa) of the boron alloyed steel B2 (X18CrMoVNbB9-1) and a conventional 12Cr-1Mo-0.23V-1W-0.1C-0.06Nb steel with bold and italics*, respectively. [Hofer *et al.*, 2002]

Figure 1.5 shows the increased creep rupture strength of 9Cr-1Mo-V-Nb-B steel, in proportion to the added boron concentration. In figure 1.6 – 1.8, creep rates decrease consistently relative to the steel without boron and also when the boron concentration is increased.

Boron alloyed steels have lower creep rates than a conventional steel without boron under each stress as shown in Figure 1.6. For a fixed concentration of boron, the difference of creep rate between steel with and without boron is almost constant, which means that boron decreases the creep rate independent of the stress level. The shape of the curve does not change - and this is also shown in Figure 1.7 (a).

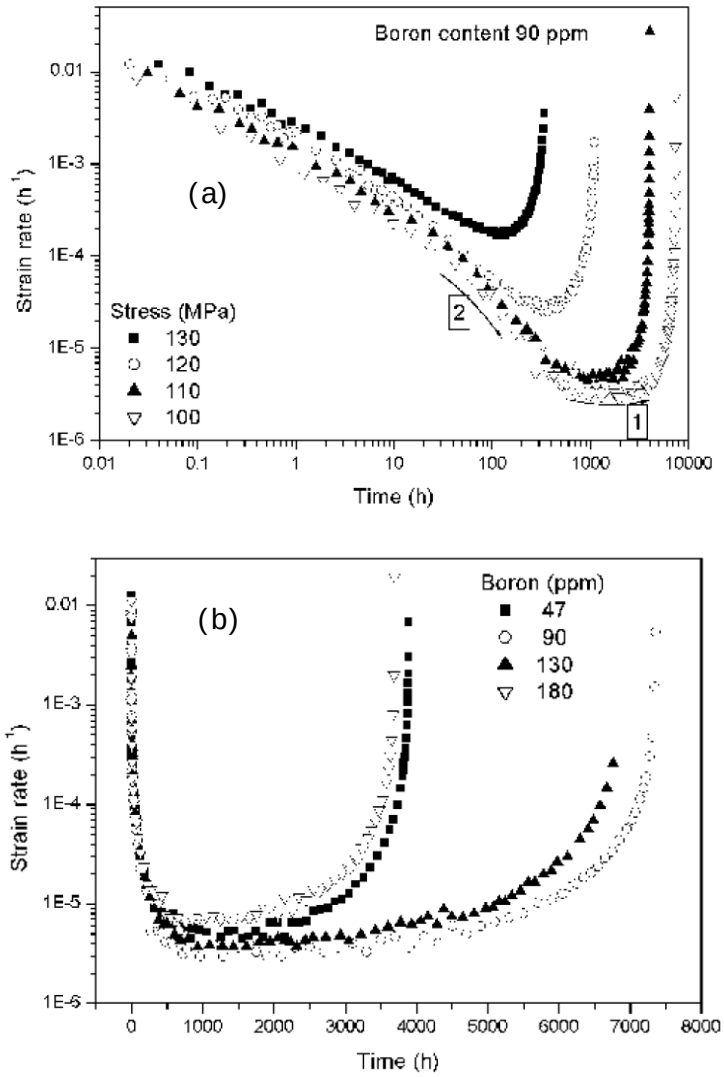

Figure 1.7 Influence of boron on the creep behavior of steel 9Cr3W3CoNbV at 650℃. Variation of creep strain rate with time (a) for 90 ppm B steel for different stress levels and (b) for steels with different B contents at 100 MPa stress.
[Albert *et al.*, 2005]

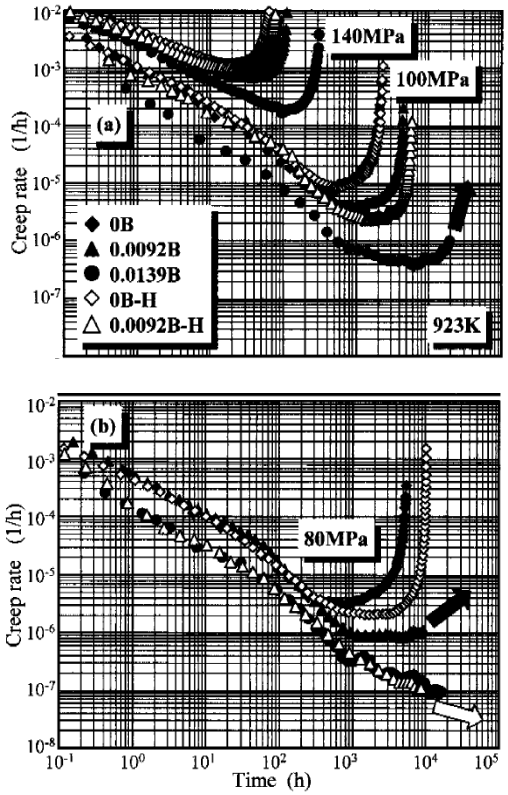

Figure 1.8 Creep rate-time curves at 923K; (a) 140 MPa and 100 MPa (b) 80 MPa. Open symbols represent the high-temperature normalizing steels.
[Horiuchi *et al.*, 2002]

The creep rate curve does change when the addition of boron concentration is increased, retarding tertiary creep by increasing the duration of the secondary creep stage as in Figure 1.7 (b). The secondary creep stage is longer when boron contents are 130 and 180 ppm than 47 and 90 ppm.

The effect of boron on creep should be significant for real applications with increasing time and decreasing stress. Although boron does not influence the

primary and tertiary creep rates, it slows down the transition from the secondary to tertiary stage which will increase the total time to rupture.

1.4. Boron and $M_{23}C_6$ Carbide

1.4.1. Carbides in Creep-resistant Steel

Graphite, M_2X, M_6C, $M_{23}C_6$, M_7C_3, Laves, *etc*. are possible precipitate phases in power plant steels. Many of them are metastable at low temperatures but it is important to understand their behavior and effects since they can nucleate easily and some of them may become stable during service. Precipitates determine the microstructure and are crucial to creep strain [Bhadeshia, 2001].

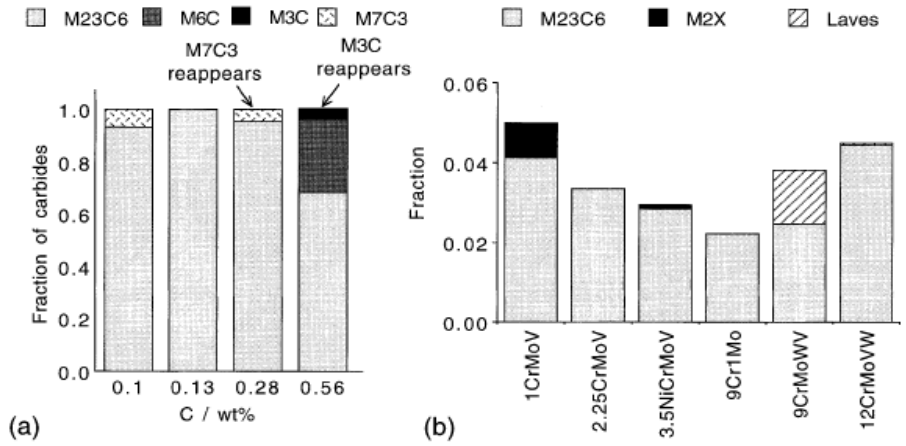

Figure 1.9 (a) Equilibrium carbides in a $2^1/_4$Cr1Mo steel as a function of the carbon concentration [Race *et al*., 1992] and (b) Equilibrium fractions of carbides in some common power plant steels. (MTDATA, SGTE database, **565** ℃). [Bhadeshia, 2001]

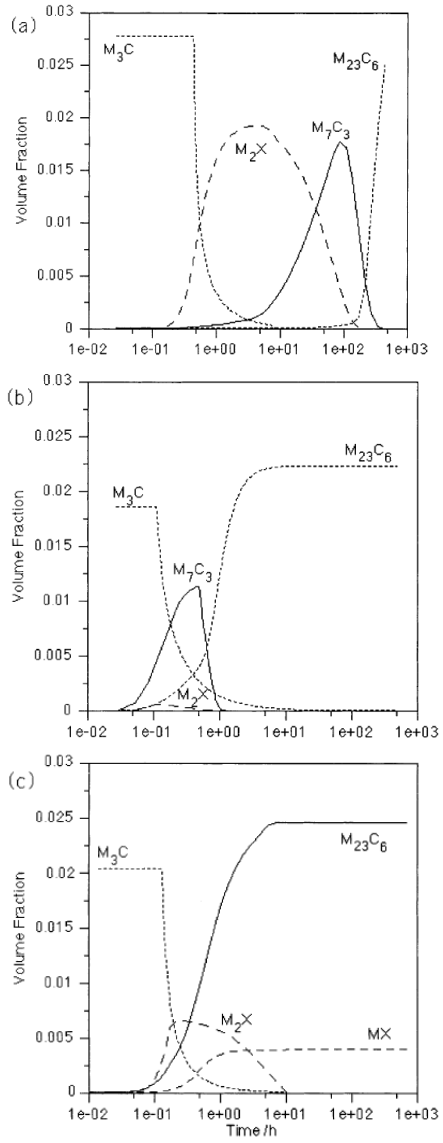

Figure 1.10 The predicted evolution of precipitate volume fractions at 600 °C for (a) $2^1/_4$Cr1Mo, (b) 3Cr1.5Mo and (c) 10CrMoV.
[Robson and Bhadeshia, 1997]

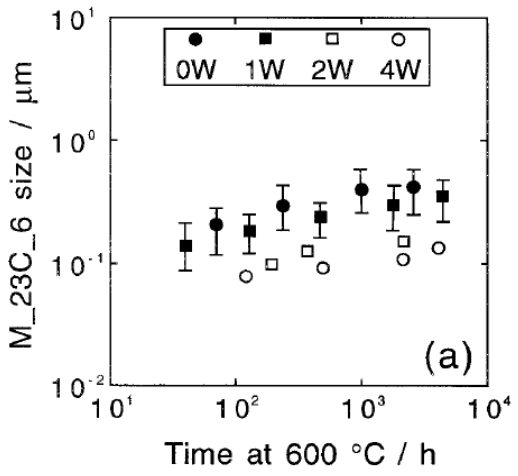

Figure 1.11 Fe-0.1C-9Cr-0.5Mn-0.3Si wt% steel tested in creep at 600 °C.

[Abe, 1999]

Although there are several carbides in creep-resistant steels and some appear and disappear before and after creep, $M_{23}C_6$ is the most common carbide. Figure 1.9 shows that $M_{23}C_6$ is obviously the majority among other carbides in equilibrium and the volume fraction of $M_{23}C_6$ does not decrease after a long time which implies its stablity after creep conditions, shown in Figure 1.10. The composition difference of the steel in Figure 1.10 (a) to (c) does influence the time of $M_{23}C_6$ appearance but it still remains as the predominant precipitate. Hence, it is possible to predict that $M_{23}C_6$ will play an important role in the creep mechanism.

Carbide particles that precipitate at the prior austenite boundaries coarsen and can easily become crack or void nucleation sites. $M_{23}C_6$ is also commonly observed in grain boundaries as coarse particles which are not helpful in preventing creep deformation [Bhadeshia, 2001]. Figure 1.11 shows the increase in the average size

of $M_{23}C_6$ as a function of time, coarsening, at the operating temperature of 600 °C and sufficient time where creep can occur. Thus it is predictable that delaying $M_{23}C_6$ precipitation or reducing its coarsening rate should increase the creep resistance.

1.4.2. Boron and $M_{23}C_6$

The influence of boron on the strength is not fully understood because of the difficulty of detecting small concentrations and locating it in the microstructure. MX, M_2X and $M_{23}C_6$ carbides are found along lath boundaries or prior austenite grain boundaries as precipitates in 9 – 12 wt% chromium steels like in Figure 1.12 [Hättestrand and Andrén, 1999; Ennis 2003].

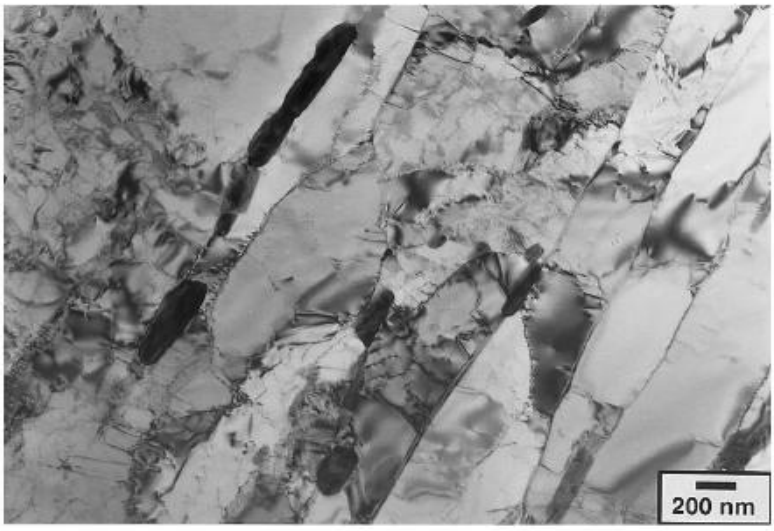

Figure 1.12 Typical microstructure of a martensitic 9 – 12 wt% chromium steel in the tempered condition. $M_{23}C_6$ carbides decorate the tempered martensite lath boundaries (TEM micrograph). [Hättestrand and Andrén, 1999]

(a)	Fe	Cr	Mn	Ni	Co	Mo	W	V	Nb	C	B	N
FB4	bal.	9.3	0.8	0.1	-	1.5	-	0.26	0.05	0.18	0.008	0.012
CB1	bal.	9.4	0.9	0.1	0.9	1.5	-	0.24	0.08	0.12	0.004	0.02
CB2	bal.	9.3	0.9	0.1	0.9	1.4	-	0.21	0.06	0.12	0.011	0.02
CD2	bal.	9.5	0.9	0.1	1.0	0.5	1.8	0.21	0.04	0.06	0.004	0.05

(b)	Fe	Cr	Mn	Ni	Co	Mo	W	V	C	B	# of ions
FB4	18.8	50.4	1.2	0.14	-	5.7	-	1.2	22.1	0.50	8004
CB1	18.1	47.4	1.3	0.11	0.07	6.2	-	1.3	24.4	0.99	2720
CB2	19.4	50.4	1.1	0.09	0.13	5.6	-	1.0	21.6	0.52	2293
CD2	17.4	50.2	1.0	0.17	0.25	1.7	4.5	0.79	23.5	0.41	2413

Table 1.4 (a) Chemical composition of investigated steels (wt%) and (b) Results from APFIM analyses of $M_{23}C_6$ carbides (at%). [Hättestrand and Andrén, 1999]

An interesting observation is that boron is enriched within $M_{23}C_6$ carbides [Lundin *et al*., 1997; Hättestrand and Andrén, 1999]. Hättestrand and Andrén did atom probe field ion microscopy (APFIM) and verified the solution of boron within $M_{23}C_6$ in ferritic creep-resistant steels.

In Table 1.4, the results of APFIM analyses of $M_{23}C_6$ and the compositions of the investigated steels are listed. $M_{23}C_6$ is chromium rich carbide, containing 50 at%, iron takes about 18 at% and boron is detected in all steels. Figure 1.13 makes clear that most of the boron is dissolved evenly in $M_{23}C_6$ carbide. Boron is distributed evenly in the phase of $M_{23}C_6$, 50 at% of Cr and 18 at% of Fe region is $M_{23}C_6$

corresponding Table 1.4.

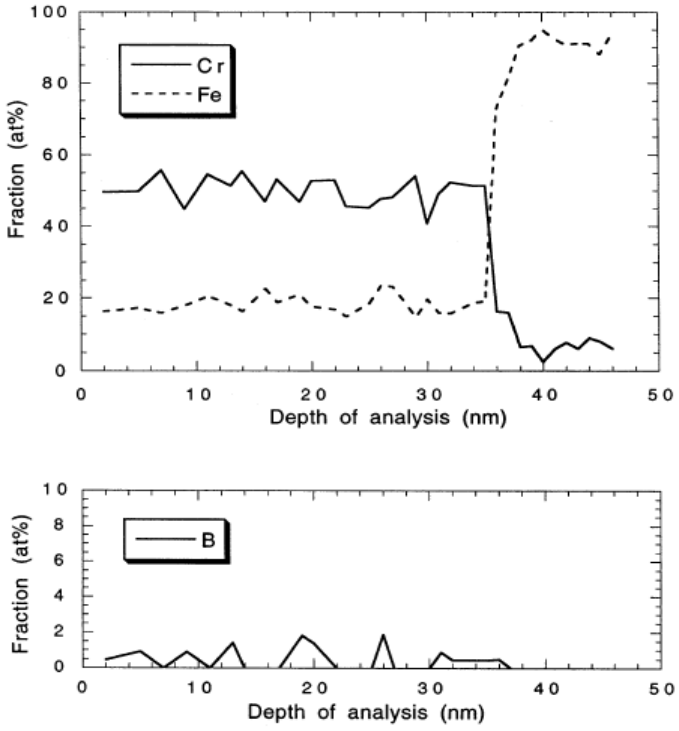

Figure 1.13 Concentration profiles across a carbide/ matrix interface in steel FB4 showing B, Fe and Cr. [Hättestrand and Andrén, 1999]

The fact that most of the boron is evenly dissolved in $M_{23}C_6$ and distribution of finer carbides implies that it may influence the stability or coarsening rate of $M_{23}C_6$, leading to increased creep strength and decreased creep rate, which has to be proven.

1.5. Previous Study on $M_{23}C_6$

To work toward the goal of understanding the role of boron in influencing the stability of $M_{23}C_6$, knowing the thermodynamic stability of $M_{23}C_6$ carbides and its various solutions at operating temperatures will be a good starting point as dissolution of boron in $M_{23}C_6$ is empirically proved (Section 1.4.2). However, to date, the thermodynamic data of $M_{23}C_6$ found in the literature or database of MTDATA does not appear in tenary phase diagrams containing boron. Thus thermodynamic data for $M_{23}(C,B)_6$ would help in understanding the phase stability of boron and $M_{23}C_6$.

Although calculations of thermodynamic properties of phases that are difficult to obtain by experiments have been conducted using first-principles methods for several decades, it is quite recent that calculations on $Cr_{23}C_6$ specifically have started due to its complex crystal structure.

1.5.1. The Structural Properties of $Cr_{23}C_6$

The crystal structure of $Cr_{23}C_6$ was determined first by X-ray diffraction and density measurements by Westgren on 1933 during work with a phase that was thought to be Cr_4C but found to be the $Cr_{23}C_6$ formula [Westgren, 1933]. It was confirmed by neutron diffraction studies [Meinhardt and Krisement, 1962] to be face-centered cubic (FCC) with space group of $Fm\bar{3}m$ having 92 chromium atoms located at Cr1(4a), Cr2(8c), Cr3(32f) and Cr4(48h) symmetry sites and 24 carbon atoms at C(24e) site. On 1972, Bowman *et al*. confirmed the structure and determined the atom positions more precisely by a neutron diffraction study of a powder sample.

Figure 1.14 and Figure 1.15 show the crystal structure of $Cr_{23}C_6$ with internal coordinates of Cr1(4a) at (000), Cr2(8c) at $(\frac{1}{4},\frac{1}{4},\frac{1}{4})$, Cr3(32f) at (*xxx*) with $x = 0.385$ and Cr4(48h) in (0*xx*) with $x = 0.165$ [Bowman *et al*., 1972]. The experimental lattice constant is known as 10.66 Å at T = 293K [Westgren, 1933; Meinhardt and Krisement, 1962; Bowman *et al*., 1972; Samson, 1953; Yakel, 1987] which decreases as the concentration of Fe in $Cr_{23}C_6$, *x* of $Cr_{23-x}Fe_xC_6$, increases up to $x \cong 7.5$ [Yakel, 1987; Kuo, 1953].

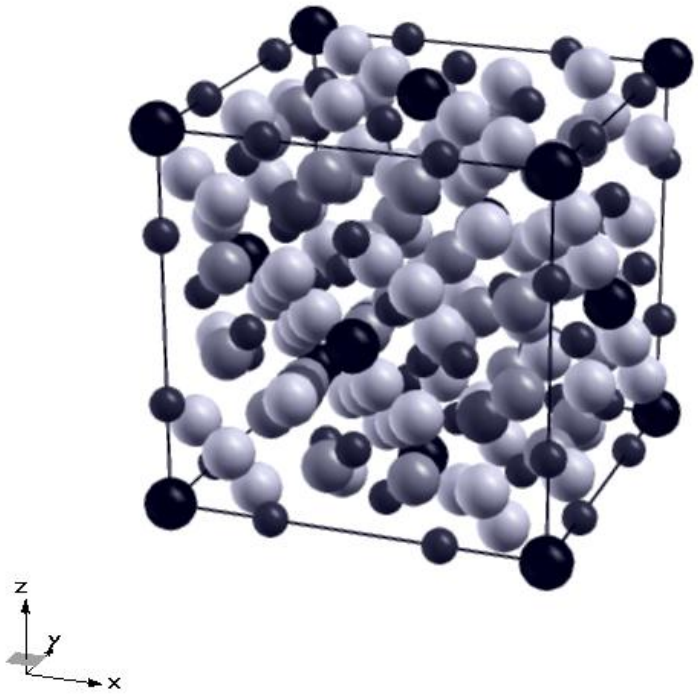

Figure 1.14 The crystal structure of $Cr_{23}C_6$ unit cell. Black, darkgrey, grey and lightgrey colored big spheres represent Cr1(4a), Cr2(8c), Cr3(32f) and Cr4(48h) respectively. Small dark grey spheres are C(24e).

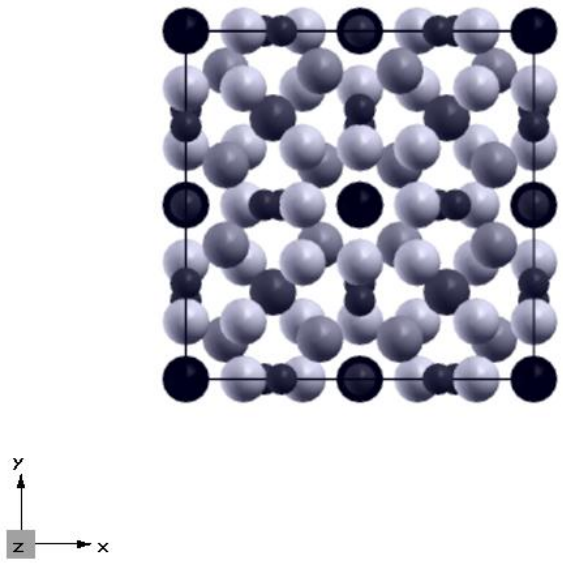

Figure 1.15 [100] projection of $Cr_{23}C_6$ unit cell in Figure 1.15.

There are four chromium sites in the unit cell by symmetry and they can be substituted by iron atoms. The site preference of Fe in $Cr_{23}C_6$ is reported as (4a), (8c), (48h) and (32f) in order since chromium at Cr1(4a) and Cr2(8c) sites have weak bonding with carbon whereas chromium at Cr4(48h) and Cr3(32f) form three and two bonding with carbon and iron replaces relatively weaker Cr-C bonds to Fe-C bonds [Yakel, 1987].

The latest atomistic study [Xie *et al*., 2005; Xie *et al*., 2006] and *ab initio* study [Santos, 2007; Jiang, 2008; Henriksson, 2008] on $Cr_{23}C_6$ obtained similar lattice constants with experiments listed in Table 1.5 with bulk modulus. The lattice parameter of the unit cell of $Cr_{23}C_6$ decreases when Cr is substituted by Fe.

	a / Å	*B* / GPa	Reference
$Cr_{23}C_6$	10.66		*[Yakel, 1987]
	10.90	275	[Xie *et al*., 2005]
	10.56	294	[Henriksson *et al*., 2008]
	10.53	298	[Jiang, 2008]
$FeCr_{22}C_6$	10.65		*[Villars and Calvert, 1991]
	10.90	278	[Xie *et al*., 2005]
$Fe^{4a}Cr_{22}C_6$	10.55		[Henriksson *et al*., 2008]
$Fe_2Cr_{21}C_6$	10.65		*[Villars and Calvert, 1991]
	10.88		[Xie *et al*., 2005]
$Fe_4Cr_{19}C_6$	10.62		*[Villars and Calvert, 1991]
	10.82		[Xie *et al*., 2005]
$Fe_{23}C_6$	10.63	276	[Xie *et al*., 2006]
$Fe_{23}B_6$	10.62		[Ohodnicki, 2008]

Table 1.5 Lattice parameter *a* and bulk modulus *B* of each system. * noted are experimental values.

1.5.2. Thermodynamic Properties of $Cr_{23}C_6$

The formation energies of $Cr_{23}C_6$, $FeCr_{22}C_6$ and $Fe_{23}C_6$ are listed in Table 1.6. Henriksson *et al*. calculated the formation energy of $Cr_{23}C_6$ and $Fe^{4a}Cr_{22}C_6$ using first-principles and showed that $Fe^{4a}Cr_{22}C_6$ is more stable than $Cr_{23}C_6$ when one chromium at Cr1(4a) site is substituted by an iron. While the formation energy of $Cr_{23}C_6$ and $FeCr_{22}C_6$ are negative, that of $Fe_{23}C_6$ is positive showing that not all chromium atoms will be substituted by iron in normal circumstances.

	ΔH / kJ atom^{-1} mol^{-1}	Reference
$Cr_{23}C_6$	-10.98	*[Kleykamp, 2001]
	-8.18	[Sandberg *et al*., 2008]
	-9.65	[Jiang, 2008]
	-8.75	[Henriksson *et al*., 2008]
$Fe^{4a}Cr_{22}C_6$	-10.65	[Henriksson *et al*., 2008]
$Fe_{23}C_6$	11.98	*[Guillermet and Grimvall, 1992]
	4.39	[Sandberg *et al*., 2008]

Table 1.6 The formation energy of each system.

* noted are experimental values.

II. First-principles Calculation

It is undeniable that the computer is one of the modern inventions that has greatly changed our lives. The rapid development and performance improvement of computers enabled researchers to do intense simulations through computer programs.

Computational physics or chemistry is a field using theories incorporated into computer programs to solve chemical and physical problems such as the calculation of structures and properties of molecules or solids. The results of this method can be approximate or accurate depending on the size of the system and the computational costs.

The *Ab initio* method is based on theory from first-principles without including any experimental data. It usually uses the Born-Oppenheimer approximation which greatly simplifies the underlying Schrödinger equation and makes the calculation easier. Through a geometry search using an energy minimization, a stable system is obtained along with all energetic properties.

Density functional theory (DFT) is a quantum mechanical theory used in physics or chemistry to investigate the electronic structure, the ground state, *etc.*, of many-body systems in particular atoms, molecules, and solids. The Schrödinger equation can be solved using the electronic density to obtain the energy eigenvalue with DFT.

To study the role of boron in stabilizing $M_{23}C_6$ carbides in creep-resistant steels, it is necessary to compare the creep-resistant properties in several alloys with different boron concentrations. The equilibrium composition of boron in $M_{23}C_6$ phase at

600 ℃ or higher can be obtained from phase diagrams if available. The problem is, $M_{23}C_6$ phase does not appear in boron phase diagrams – calculated nor experimental thermodynamic data exist. Hence, for the first step, calculation of thermodynamic data such as formation enthalpies is inevitable.

First-principles calculations, especially using the all-electron total-energy full potential linearized augmented plane wave (FLAPW) method [Wimmer *et al*., 1981; Weinert *et al*., 1982] within the density functional theory is used to calculate the properties of Fe and B substituted $M_{23}C_6$,. Although there exists a limitation that these calculation results are based on 0 K and zero pressure, it is definitely the best way to approach without experimental information.

2.1. Theoretical Background

Introduced at 1929, the Schrödinger equation [1926] describes how the quantum state of a physical system changes in time. Attention had been focused on solving the Schrödinger equation for decades but the complexity of the system made this difficult. It was in 1964 when Hohenberg and Kohn [1964] proved a theorem which provided an alternative way to solve the Schrödinger equation,

$$H\Psi = E\Psi \qquad \text{Eq. (2.1)}$$

where H is the Hamiltonian operator and Ψ is the wave function of the Schrödinger equation.

2.1.1. Many-body Hamiltonian

The Hamiltonian of a solid consists of the kinetic of the nuclei and electrons, T_n and T_e, respectively, the interactions between the nuclei and electrons and the interaction between nuclei and electrons, V_{n-n}, V_{e-e} and V_{n-e}, respectively.

$$H = T_n + T_e + V_{n-n} + V_{e-e} + V_{n-e}\,. \qquad \text{Eq. (2.2)}$$

Eq. (2.2) can be written in Hartree atomic unit, as

$$H = -\sum_i \frac{1}{2}\nabla_i^2 + \frac{1}{2}\sum_{i\neq j}\frac{1}{|\boldsymbol{r}_i - \boldsymbol{r}_j|} - \sum_I \frac{1}{2M_I}\nabla_I^2 + \frac{1}{2}\sum_{I\neq J}\frac{Z_I Z_J}{|\boldsymbol{R}_I - \boldsymbol{R}_J|} - \sum_{i,I}\frac{Z_I}{|\boldsymbol{r}_i - \boldsymbol{R}_I|}, \qquad \text{Eq. (2.3)}$$

where indices of electrons and nuclei are i, j and I, J respectively, the mass and charge of the *I*-th lattice nuclei are M_I and Z_I respectively and $\boldsymbol{R} = \{\boldsymbol{R}_1, \ldots, \boldsymbol{R}_N\}$ and $\boldsymbol{r} = \{\boldsymbol{r}_1, \ldots, \boldsymbol{r}_N\}$ denote the state of all nuclei and electrons in the solid, respectively. This Hamiltonian of Eq. (2.3) is subject to the Schrödinger equation of Eq. (2.1)

$$H\,\Psi(\boldsymbol{R}, \boldsymbol{r}) = E\,\Psi(\boldsymbol{R}, \boldsymbol{r}), \qquad \text{Eq. (2.4)}$$

where $\Psi(\boldsymbol{R}, \boldsymbol{r})$ is the normalized eigenfuction of the Hamiltonian.

2.1.2. Born-Oppenheimer Approximation

The Born-Oppenheimer approximation or the adiabatic approximation [Born, 1926; Born and Oppenheimer, 1930; Jost and Pais, 1951; Kohn, 1954] allows to decouple the Schrödinger equation into the electronic and nuclear components.

$$\Psi_{\text{total}} = \Psi_{\text{electrons}} \times \Psi_{\text{nuclei}}. \qquad \text{Eq. (2.5)}$$

This is because of the mass difference of electrons and nuclei. Since the mass of

nuclei of the solid are heavy with respect to that of the electrons, the nuclei are not much altered by the movement of the electrons. However, since the electrons respond to the motion of nuclei adiabatically, it is possible to fix the positions of the lattice nuclei approximately with respect to the motions of the electrons.

Eq. (2.4) can be solved approximately separating the electrons and nuclei part, and the following Eq. (2.6) and Eq. (2.7) represent the adiabatic approximation of the solid.

$$(T_e + V_{e_e} + V_{n_e}(\boldsymbol{R}))\ \Psi_{\text{electrons}} = E_e(\boldsymbol{R})\,\Psi_{\text{electrons}}. \qquad \text{Eq. (2.6)}$$

$$(T_n + V_{n-n} + E_e(\boldsymbol{R}))\ \Psi_{\text{nuclei}} = E\,\Psi_{\text{nuclei}}. \qquad \text{Eq. (2.7)}$$

Most problems in solid state physics are reduced to Eq. (2.6), *N*-electrons with a given static nucleus alignment in a solid.

2.1.3. Many-electron System

The many-electron wave function can be approximated to a product of single particle functions,

$$\Psi(\boldsymbol{r}_1, \ldots, \boldsymbol{r}_N) = \Psi(\boldsymbol{r}_1) \cdots \Psi(\boldsymbol{r}_N). \qquad \text{Eq. (2.8)}$$

Each Ψ_i satisfies a single-electron Schrödinger equation

$$\left[-\frac{1}{2}\nabla_i^2 + V_{ext} + \Phi_i\right] \Psi_i(\boldsymbol{r}) = \boldsymbol{\varepsilon_i}\,\Psi_i(\boldsymbol{r}) \qquad \text{Eq. (2.9)}$$

where V_{ext} is the external potential and Φ_i is the Coulumb potential given by Poisson's equation,

$$\nabla^2 \Phi_i = 4\pi \sum_{j=1, j\neq i}^{N} |\Psi_i|^2. \qquad \text{Eq. (2.10)}$$

2.2. Density Functional Theory

Density functional theory uses spatially dependent electron theory to determine the properties of a many-electron system.

2.2.1. Hohenberg-Kohn Theorem

Density functional theory starts from Hohenberg and Kohn [1964], first demonstrating that the ground state properties of a many-electron system are uniquely determined by an electron density that depends on only 3 spatial coordinates and second defining the energy functional for the system.

The Hamiltonian of *N* electrons moving in an external potential $V_{ext}(\boldsymbol{r})$ is,

$$H = T + V_{e-e} + \sum_{i}^{N} V_{ext}(\boldsymbol{r_i}) \qquad \text{Eq. (2.11)}$$

where T is kinetic and V_{e-e} is the interaction between electrons. The electron density $n(\boldsymbol{r})$ can be obtained using the functional defined by Levy [1979],

$$F[n] = \min_{\varphi \to n} < \varphi | T + V_{e-e} | \varphi > \qquad \text{Eq. (2.12)}$$

where the minimum is taken over all $\varphi(\boldsymbol{r})$ which is antisymmetric wave function that give the density n. $F[n]$ is universal since it does not refers to any specific systems nor the external potential.

Let E_{GS}, φ_{GS} and $n_{GS}(\boldsymbol{r})$ be the ground-state energy, wave function and density, respectively. Then the total energy E which can be expressed in terms of a density functional, $E[n]$,

$$E[n] = \int \mathrm{d}\boldsymbol{r} V_{ext}(\boldsymbol{r}) n(\boldsymbol{r}) + F[n] \geq E_{GS} \qquad \text{Eq. (2.13)}$$

by a variational principle, for all *n*-representable $n(\boldsymbol{r})$.

$$\int \mathrm{d}\boldsymbol{r} V_{ext}(\boldsymbol{r}) n_{GS}(\boldsymbol{r}) + F[n_{GS}] = E_{\mathrm{GS}}. \qquad \text{Eq. (2.14)}$$

2.2.2. Kohn-Sham Equation

The Kohn-Sham equation is the Schrödinger equation of a fictitious system of non-interacting particles which are typically electrons that generate the same density as any given system of interacting particles, in DFT.

The total kinetic energy of the non-interacting electron system with density n is a density functional by Hohenberg and Kohn theorem,

$$T = T[n]. \qquad \text{Eq. (2.15)}$$

Introduced by Kohn and Sham [1965], Eq. (2.13) with Eq. (2.12) ca be rewritten as,

$$E[n] = T[n] + \int \mathrm{d}\boldsymbol{r} n(\boldsymbol{r})[V_{ext}(\boldsymbol{r}) + V_c(\boldsymbol{r})] + E_{XC}[n], \qquad \text{Eq. (2.16)}$$

where $V_c(\boldsymbol{r})$ is the classical Coulomb potential for electrons and E_{XC} is the exchange-correlation functional which determines the degree of the approximation.

$E[n]$ should have minium value at ground state electron density and by applying the variational principle to Eq. (2.16),

$$\frac{E[n]}{\delta n} = \frac{T[n]}{\delta n} + V_{ext}(\boldsymbol{r}) + V_c(\boldsymbol{r}) + \frac{E_{XC}[n]}{\delta n} = \mu, \qquad \text{Eq. (2.17)}$$

where μ is the Lagrange multiplier associated with the requirement for the particle number conservation. For a corresponding system of N non-interacting fictitious particles moving in an external effective potential V_{eff} which gives the same

energy of the considering electronic system but without inter-particle interactions,

$$\frac{E[n]}{\delta n} = \frac{T[n]}{\delta n} + V_{eff}(\boldsymbol{r}) = \mu. \qquad \text{Eq. (2.18)}$$

Comparing Eq. (2.17) and Eq. (2.18), the external effective potential is given by

$$V_{eff}(\boldsymbol{r}) = V_{ext}(\boldsymbol{r}) + V_c(\boldsymbol{r}) + \frac{E_{XC}[n]}{\delta n}. \qquad \text{Eq. (2.19)}$$

The solution of Eq. (2.19) can be found by solving the Schrödinger-like equation for a single noninteracting particle,

$$\left[-\frac{1}{2}\nabla^2 + V_{eff}\right] \Psi_i(\boldsymbol{r}) = \boldsymbol{\varepsilon_i}\, \Psi_i(\boldsymbol{r}), \qquad \text{Eq. (2.20)}$$

which yields the density

$$n(\boldsymbol{r}) = \sum_{i=1}^{N} |\, \Psi_i(\boldsymbol{r})|^2. \qquad \text{Eq. (2.21)}$$

2.2.3. Exchange-Correlational Functional

The exchange-correlational functional term E_{XC} describes the many electron exchange and correlation effects but is not known except in simple cases such as the homogeneous electron gas. Therefore, for real systems, approximations are used. The local density approximation (LDA) suggested by Hedin and Lundqvist [1971] is the most widely used approximation that depends solely upon the value of the electronic density at each point in space. LDA provides a realistic description of the atomic structure, elastic and vibrational properties for a wide range of systems but not reliable enough to describe the energetics of chemical reactions, such as reaction enthalpies and activation energy barriers.

The more recent generalized gradient approximations (GGA) [Perdew *et al*., 1996] is computationally simple as LDA and have overcome such deficiencies to a large extent giving a more realistic account of energy barriers and adsorption energies for molecules on metal or semiconductor surfaces. The general form of exchange-correlational functional of GGA is,

$$E_{XC}^{GGA}[n(\boldsymbol{r})] = \int f\big(n(\boldsymbol{r}), \nabla n(\boldsymbol{r})\big)\mathrm{d}\boldsymbol{r}. \qquad \text{Eq. (2.22)}$$

2.3. The Full-Potential Linearized Augmented Plane-Wave (FLAPW) Method

The problem of solving many electron problems has been changed to an eigenvalue problem of single particle Kohn-Sham equation,

$$\left[-\frac{1}{2}\nabla^2 + V_{ext}(\boldsymbol{r}) + V_c(\boldsymbol{r}) + \frac{E_{XC}[n]}{\delta n}\right]\Psi_i(\boldsymbol{r}) = \boldsymbol{\varepsilon_i}\,\Psi_i(\boldsymbol{r}). \qquad \text{Eq. (2.23)}$$

Figure 2.1 shows an overview of electronic structure methods proposed for solving Eq. (2.23) for different applications, geometries, symmetries, chemical elements and materials requiring different approximations [Blügel, 2006].

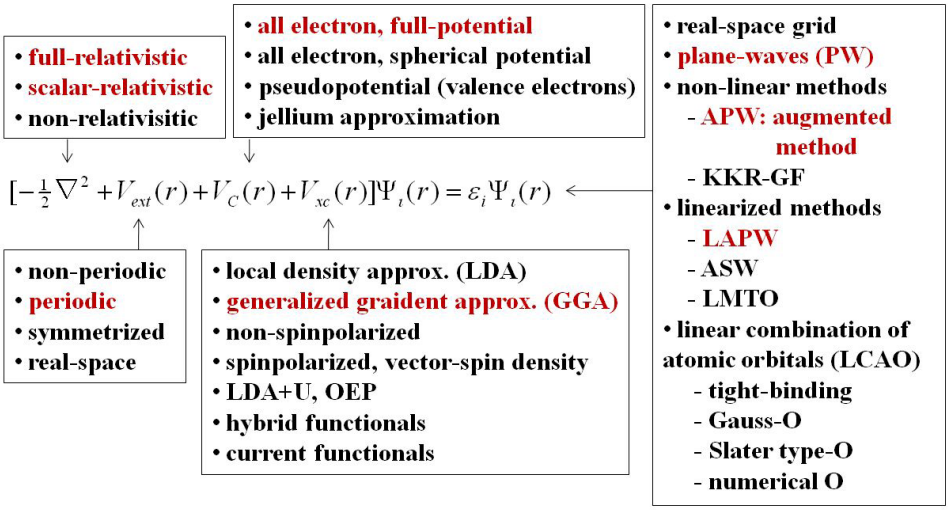

Figure 2.1 Overview of electronic structure calculations [Blügel, 2006].

The full-potential spin-polarized linearized augmented plane wave (FLAPW) method is presently one of the most accurate electronic structure calculation schemes. It has its origin in the augmented plane wave (APW) method introduced by Slater [1937]. The APW method is demanding computationally since the basis functions are energy dependent and the eigenvalue problem is non-linear.

In the FLAPW method there is no shape approximation for either the charge density or the potential, and all electrons are treated self-consistently [Jansen and Freeman, 1984; Wimmer et al., 1981; Singh, 1994; Freeman and Wimmer, 1995]; the core electrons are treated fully relativistically and the valence electrons are treated semi-relativistically.

In the FLAPW method, the real space within a unit cell is partitioned into spherical regions around atoms, “muffin-tins (MT)”, and interstitial regions between the spheres in bulk materials. Plane waves are used in the interstitial region and in the spherical regian the basis functions are products of radial functions and spherical harmonics.

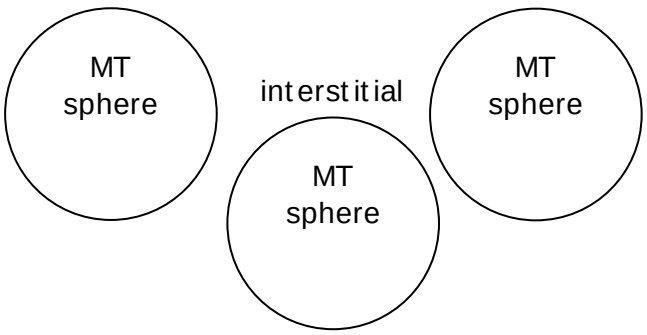

Figure 2.2 The space division in the FLAPW method.

2.4. Computational Method

The Kohn-Sham equation [Kohn and Sham, 1965] was solved self-consistently by the all-electron total-energy full potential linearized augmented plane wave (FLAPW) method [Wimmer *et al*., 1981; Weinert *et al*., 1982] implemented in the QMD-FLAPW package within the generalized gradient approximation [Perdew *et al*., 1996] to density functional theory [Hohenberg and Kohn, 1964]. The integration over the three dimensional Brillouin zone (3D-BZ) was performed by the improved tetrahedron method [Lee *et al*., 2002] over a $9 \times 9 \times 9$ for $M_{23}(B,C)_6$, $17 \times 17 \times 17$ for graphite and ferromagnetic BCC Fe and $19 \times 19 \times 19$ for anti-ferromagnetic Cr and a $\alpha-$boron Monkhorst-Pack mesh [Monkhorst and Pack, 1976] in the 3D-BZ. The corresponding number of k-points are 35 for $Cr_{23}C_6$, $Fe^{4a}Cr_{22}C_6$, $Fe^{8c}Cr_{22}C_6$, $Fe_{23}C_6$, $Cr_{23}B_6$ and $Fe_{23}B_6$, 75 for $Cr_{23}C_5B$, 85 for $Fe^{32f}Cr_{22}C_6$, 125 for $Fe^{48h}Cr_{22}C_6$, 279 for ferromagnetic body-centered cubic Fe, 220 for anti-ferromagnetic body-centered cubic C, 297 for graphite and 670 for alpha boron.

The linearized augmented plane wave (LAPW) basis set was expanded using a plane wave cutoff of $4.69\ (2\pi/a)$, where a is the corresponding lattice constant. Lattice harmonics with $l \leq 10$ were employed to expand the charge density, potential, and wave functions inside each muffin-tin (MT) sphere, with the radii of 2.1 a.u. for Cr and Fe and 1.6 a.u. for C and B. The star-function cutoff of $14.07\ (2\pi/a)$ was employed for depicting the charge density and potential in the interstitial region. The chosen computational parameters were carefully checked for

convergency [Seo *et al*., 2009]. The core electrons were treated fully relativistically while valence states were treated scalar relativistically without spin-orbit coupling. Self-consistency was assumed when the difference between input and output charge (spin) density was less than 1.0×10^{-5} electrons/a.u.^{3} The equilibrium volume and bulk modulus are obtained by fitting to the universal equation of state [Vinet *et al*., 1989].

Each $(Fe,Cr)_{23}(C,B)_6$ system is optimized with respect to its lattice parameter and internal atomic coordinates and relaxed using first-principle calculations. Obtained total energy is the internal energy *U* at zero Kelvin and zero pressure. The formation enthalpy ΔH at zero Kelvin and zero pressure is the calculated internal energy ΔU as and product of volume *V* and external pressure *P* vanish at zero pressure. The formation enthalpy of a ternary compound $X_lY_mZ_n$, $\Delta H_f(X_lY_mZ_n)$, is

$$\Delta H(X_lY_mZ_n) = \{H(X_lY_mZ_n) - lH(X) - mH(Y) - nH(Z)\}/(l+m+n)$$
$$= \{U(X_lY_mZ_n) - lU(X) - mU(Y) - nU(Z)\}/(l+m+n) \qquad \text{Eq. (2.24)}$$

where X, Y and Z are elements and *l*, *m* and *n* are the number of X, Y and Z atoms, respectively.

III. Results and Discussions

$Cr_{23}C_6$ and its various solid solutions are vital phasesin the design of most modern of creep-resistant steels. The role of boron, in increasing the creep resistance by influencing $M_{23}C_6$ carbide has been reviewed in chapter 1. Although there has been a great deal of work in understanding the significance of $M_{23}C_6$ with respect to elevated temperature properties, the detailed thermodynamic properties deserve further attention. In particular, there is a long-term need to establish the distribution of atoms within the unit cell, energetic and structural implications of different atoms in the basic $Cr_{23}C_6$ crystal structure, including solutes such as iron and boron. The standard thermodynamic assessments which are based on macroscopic measurements do not reveal such information. To work towards this goal, the all-electron total-energy FLAPW method within the generalized gradient approximation is used as discussed in chapter 2.

There have recently been several calculations relating to $M_{23}C_6$ carbides. They are, however, largely based on empirical atomic potentials or pseudopotential treatments. The all-electron treatment was done by Santos [2007], but the crystal structure was modeled as a simplified four chromium atomic basis face centered cubic (FCC) structure, Cr_4C. Moreover, calculations on $M_{23}(B,C)_6$ are hard to find and it is impossible to obtain the effect of boron within this structure. Hence, it is necessary to obtain reliable and consistent results by all-electron treatments for this crystal structure.

3.1. Lattice Parameter Optimization

$M_{23}C_6$ carbide basically follows the crystal structure of $Cr_{23}C_6$ (Figure 1.14). Starting from the lattice constants and internal coordinates in [Bowman *et al*., 1972], the unit cell volume with minimum energy is found by fitting to the universal equation of state [Vinet *et al*., 1989]. The internal atomic positions are relaxed by using the total energy and force minimization scheme based on the Broyden method. When the force on each atom is smaller than 2mRy/a.u. and the position does not change more than 3×10^{-3} a. u., it is considered as a relaxed structure.

	Calculated		Literature [Table 1.5]
	a / Å	V / Å^3	a / Å
$Cr_{23}C_6$	10.57	295	10.53 ~ 10.90
$Fe^{4a}Cr_{22}C_6$	10.56	294	10.55
$Fe^{8c}Cr_{22}C_6$	10.57	295	
$Fe^{32f}Cr_{22}C_6$	10.56	294	
$Fe^{48h}Cr_{22}C_6$	10.56	294	
$Fe_{23}C_6$	10.48	288	10.63
$Fe_{23}B_6$	10.62	299	10.62
$Cr_{23}B_6$	10.72	308	
$Cr_{23}C_5B$	10.60	297	

Table 3.1 The calculated lattice parameter and volume of the unit cell of $M_{23}(C,B)_6$. Literature values are from Table 1.5. $Fe^ACr_{22}C_6$ is structure with Cr replaced by Fe at A site.

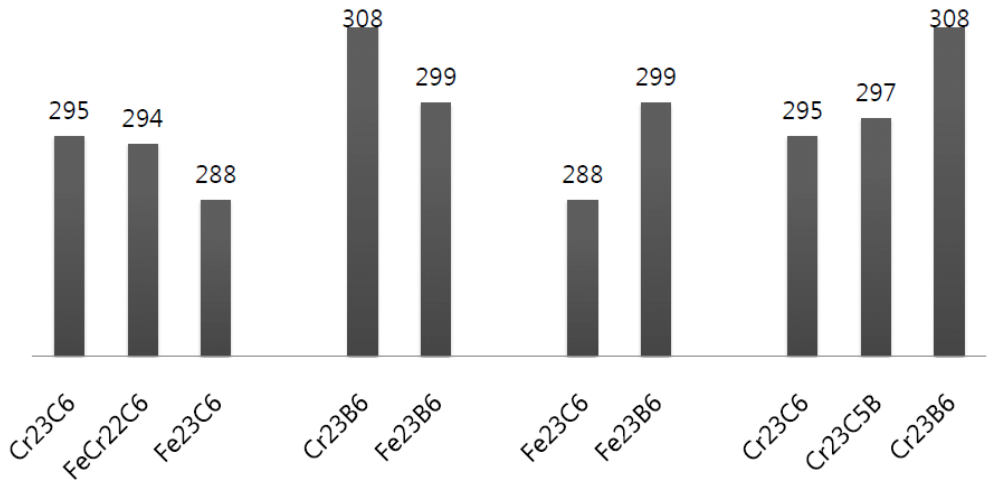

Figure 3.1 Bar chart of Table 3.1. The value on the top of each bar is the unit cell volume (Å^3) of the system.

	Relaxed (Calculated)			[Bowman *et al*., 1972]		
	x	y	z	x	y	z
Cr1(4a)	0	0	0	0	0	0
Cr2(8c)	0.25	0.25	0.25	0.25	0.25	0.25
Cr3(32f)	0.381	0.381	0.381	0.385	0.385	0.385
Cr4(48h)	0	0	0.34	0	0	0.33
C(24e)	0.276	0.276	-0.276	0.275	0.275	-0.275

Table 3.2 The calculated relaxed internal fractional coordinates of $Cr_{23}C_6$.

Tables 3.1 and 3.2 show the equilibrium lattice parameter of $Cr_{23}C_6$ which is 10.57 Å in the nonmagnetic (NM) state with calculated relaxed coordinates compared with experimental values. The calculated lattice constant is 0.8% smaller than the experimental data 10.65~10.66Å, an excellent agreement given that the measurements are at ambient temperature whereas the first-principles calculations are for 0 K and zero pressure. The calculated, relaxed, internal coordinates of atoms in $Cr_{23}C_6$ also match to the experimental internal coordinates. These coordinates are used in all of the other $M_{23}(C,B)_6$ structure calculations, $Cr_{23}B_6$, $Fe_{23}C_6$, $Fe_{23}B_6$ and $FeCr_{22}C_6$, and the relaxed results are all similar to those in Table 3.2.

The calculated interatomic distances of NM $Cr_{23}C_6$ are listed in Table 3.3. We started from the experimental internal coordinates (Table 3.2) and relaxed the internal coordinates to the most stable total energy. Comparing Tables 3.2 and 3.3, it is noticeable that Cr3(32f), Cr4(48h) and C(24e) moved slightly from the experimental positions. Cr3(32f) moves closer to Cr1(4a) and Cr2(8c) far from C(24e), Cr4(48h) moves closer to Cr2(8c) and far from Cr1(4a) and C(24e), and the interatomic distance between Cr3(32f) and Cr4(48h) decreases. But the movement of internal coordinates after relaxation is too small to deduce it to be related to bonding between atoms and their reactions.

Atomic site	Neighboring Atoms	Coordination Numbers	Calculated d (Å)		Experimental d (Å)	
			NM	PNM	Ref. (a)	Ref. (b)
Cr1(4a)	Cr4	12	2.469	2.543	2.558	2.561
	C	6	2.909	2.924		2.933
Cr2(8c)	Cr3	4	2.474	2.401	2.415	2.437
	Cr4	12	2.933	2.903	2.923	2.926
Cr3(32f)	Cr2	1	2.474	2.401		2.437
	Cr3	3	2.433		2.536	2.516
	Cr4	6	2.679	2.619	2.637	2.646
	C	3	2.077	2.097	2.110	2.113
Cr4(48h)	Cr1	1	2.469	2.543	2.558	2.561
	Cr2	2	2.933	2.903	2.923	2.926
	Cr3	4	2.679	2.619	2.637	2.646
	Cr4	1	2.469		2.414	2.415
	C	2	2.098	2.121	2.136	2.130
C	Cr1	1	2.909	2.924		2.933
	Cr3	4	2.077	2.097	2.110	2.113
	Cr4	4	2.098	2.121	2.136	2.130

Table 3.3 The atom coordinates and calculated interatomic distance *d* in units of Å of $Cr_{23}C_6$. NM – nonmagnetic, RNM - Relaxed NM

Ref. (a) [Bowman *et al.*, 1972] Ref. (b) [Yakel, 1987]

3.1.1. Effect of Fe and B Substitution

As seen from the data in Table 3.1 and Figure 3.1, Fe substitution into a chrominum site decreases the lattice parameter and cell volume of $M_{23}(B,C)_6$ and B substitution into a carbon site has the opposite effect. The unit cell volume of $FeCr_{22}C_6$ and $Fe_{23}C_6$ decreases 0.3 % and 2.4 % respectively relative to $Cr_{23}C_6$ and the volume of $Fe_{23}B_6$ decreases 2.9 % when compared with $Cr_{23}B_6$. The unit cell volume of $Cr_{23}(C_5B)$ and $Cr_{23}B_6$ increases 0.7 % and 4.4 % respectively relative to $Cr_{23}C_6$ and that of $Fe_{23}B_6$ increases 3.8 % when compared with $Fe_{23}C_6$.

3.2. The Formation Enthalpy

The formation enthalpy at zero Kelvin (ΔH) of $Fe_xCr_{23-x}C_{6-y}B_y$ system, where x and y are the numbers of Fe and B atoms in the structure respectively, was calculated using first-principles to compare the thermodynamic properties when Fe and B are substituted into $Cr_{23}C_6$. Each $Fe_xCr_{23-x}C_{6-y}B_y$ system was optimized with respect to its lattice parameter and internal atomic coordinates and relaxed using first-principles calculations as in Table 3.1.

The formation enthalpies of each $Fe_xCr_{23-x}C_{6-y}B_y$ system at zero Kelvin and zero pressure calculated using Eq. (2.24) and the results are presented in Table 3.4 and Figure 3.2. The most stable structure among calculated phases is $Fe_{23}B_6$ with the formation enthalpy of -17.11 kJ atom-mol^{-1}, 8.5 kJ atom-mol^{-1} lower than $Cr_{23}C_6$. Only $Fe_{23}C_6$ has positive formation enthalpy, consistent with experimental [Guillermet and Grimvall, 1992] and calculated [Sandberg *et al*., 2008] data.

Figure 3.3 shows that the formation enthalpy of $Fe_xCr_{23-x}C_6$ does not linearly increase or decrease with increasing Fe concentration. $Cr_{23}C_6$ is stabilized only when Fe is substituted to Cr1(4a) site, and Fe substitution to other sites makes it less stable. The curve connecting the enthalpies of $Cr_{23}C_6$, $Fe^{4a}Cr_{22}C_6$ and $Fe_{23}C_6$ in Figure 3.3 is fitted using a second order polynomial and the minimum is around $x_{\mathrm{Fe}} \approx 0.4$ which corresponds to about 9 atoms of Fe. It can therefore be deduced that $x \approx 9$ in $Fe_xCr_{23-x}C_6$ may stabilize the structure. Though it will be possible to measure the optimum Fe concentration in $Fe_xCr_{23-x}C_6$ with more investigations, the APFIM results of Table 1.3 [Hättestrand and Andrén, 1999]

show that there are about 14 Cr atoms and 5~6 Fe atoms on average in $M_{23}C_6$. Therefore Fe atoms could also take any of 2 Cr2(8c), 8 Cr3(32f) and 12 Cr4(48h) sites of $M_{23}C_6$ in steel.

	ΔH / kJ atom-mol^{-1}	
	Calculated	Literature
$Cr_{23}C_6$	-8.61	-10.98 ~ -8.18
$Fe^{4a}Cr_{22}C_6$	-10.43	-10.65
$Fe^{8c}Cr_{22}C_6$	-7.47	
$Fe^{32f}Cr_{22}C_6$	-7.63	
$Fe^{48h}Cr_{22}C_6$	-7.99	
$Fe_{23}C_6$	3.66	4.39 ~ 11.98
$Fe_{23}B_6$	-17.11	
$Cr_{23}B_6$	-13.53	
$Cr_{23}C_5B$	-9.74	

Table 3.4 The calculated formation enthalpy ΔH of $M_{23}(C,B)_6$. Literature values are from Table 1.5.

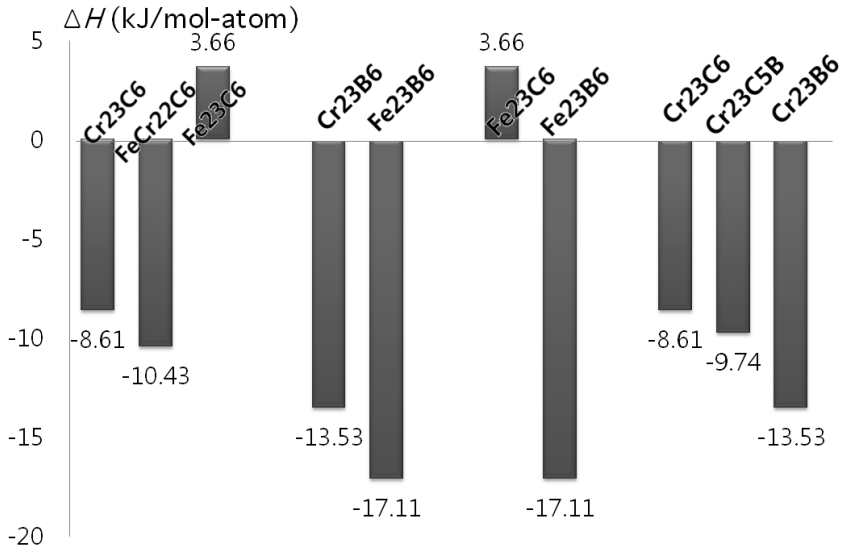

Figure 3.2 The calculated formation enthalpy ΔH of $M_{23}(C,B)_6$.

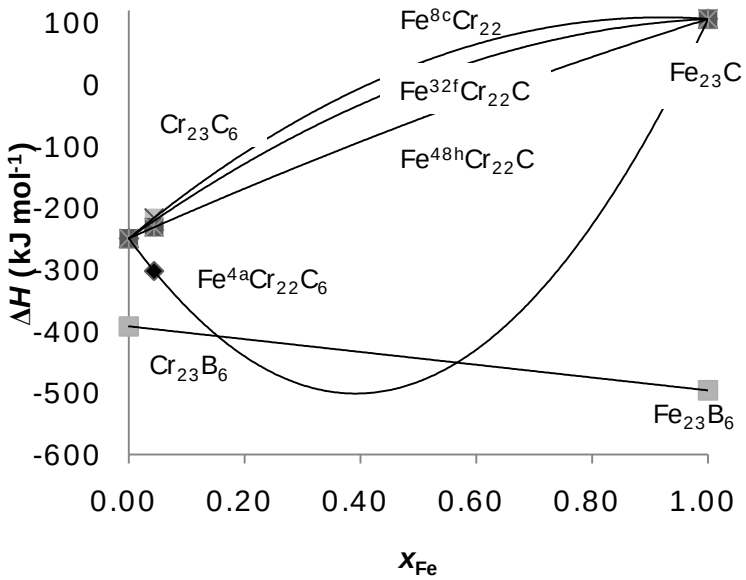

Figure 3.3 The calculated formation enthalpy ΔH of $M_{23}C_6$ and $M_{23}B_6$ versus Fe concentration.

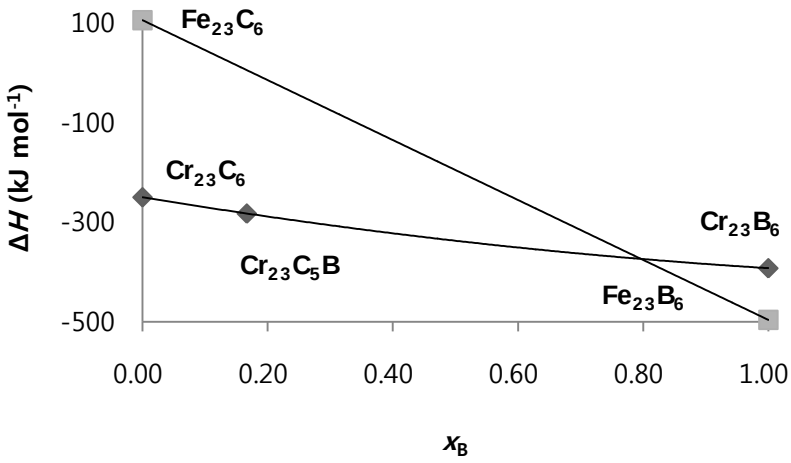

Figure 3.4 The calculated formation enthalpy ΔH_f of $Cr_{23}(B,C)_6$ and $Fe_{23}(B,C)_6$ versus B concentration.

Figure 3.4 shows the formation enthalpy of $M_{23}C_6$ is decreasing by boron substitution into carbon sites. Boron stabilizes $M_{23}C_6$ by dissolving in it. This may also explain the mechanism by which boron retards the coarsening rate of $M_{23}C_6$ observed experimentally – it makes it more thermodynamically stable.

In spite of the fact that, the calculated formation enthalpies here have limitations, zero Kelvin and zero pressure, this is meaningful as it is the first consistent data that provides sufficiently comparable systems of $M_{23}C_6$ with Fe and B solutes.

Now the results should be implemented to thermodynamic database to calculate the phase diagrams at operating temperatures for further investigations. In particular, it is not possible to comment in detail about coarsening without considering the equilibrium between the carbide and tempered martensitic matrix.

3.3. Bulk Moduli

Table 3.5 contains the calculated bulk moduli of $(Cr,Fe)_{23}(C,B)_6$ systems with comparison against literature data. The calculated bulk moduli of $Cr_{23}C_6$ and $Fe^{4a}Cr_{22}C_6$ agree reasonably with the previous calculations and the calculated nor experimental bulk moduli for other boron substituted $Cr_{23}(B,C)_6$ are not founded in literatures.

This result will give consistent information on changes of bulk modulus by Fe and B substitution in $Cr_{23}C_6$. The bulk modulus of ferromagnetic (FM) $Fe_{23}C_6$ and $Fe_{23}B_6$ (Table 3.6) are 206 GPa and 196 GPa respectively which are 28 % and 25 % lower than the bulk modulus of NM $Cr_{23}C_6$ and $Cr_{23}B_6$. The bulk modulus of nonmagnetic $Cr_{23}B_6$ and FM $Fe_{23}B_6$ are 260 GPa and 196 GPa respectively which are 9 % and 5 % lower than the bulk modulus of NM $Cr_{23}C_6$ and FM $Fe_{23}C_6$.

The bulk modulus is reduced when Cr is substituted by Fe and also reduced when C is substituted by B.

	B / GPa	
	Calculated	Literature
$Cr_{23}C_6$	286	275 ~ 298
$Fe^{4a}Cr_{22}C_6$	287	278
$Fe^{8c}Cr_{22}C_6$	277	
$Fe^{32f}Cr_{22}C_6$	289	
$Fe^{48h}Cr_{22}C_6$	289	
$Fe_{23}C_6$	206	
$Fe_{23}B_6$	196	
$Cr_{23}B_6$	260	
$Cr_{23}C_5B$	283	

Table 3.5 The calculated bulk modulus *B* of $M_{23}(C,B)_6$. Literature values are from Table 1.4.

3.4. Magnetic Properties

Table 3.6 summerises the calculated total magnetization per unit cell in units of T(Tesla) of $(Cr,Fe)_{23}(C,B)_6$ systems. By calculated results, $Cr_{23}C_6$, $Cr_{23}B_6$ and $Cr_{23}C_5B$ are nonmagnetic and $Fe_{23}C_6$ and $Fe_{23}B_6$ are ferromagnetic. The magnetic state did not changed by one Fe atom substitution to $Cr_{23}C_6$.

	Total (T)
$Fe^{4a}Cr_{22}C_6$	0.00
$Fe^{8c}Cr_{22}C_6$	0.04
$Fe^{32f}Cr_{22}C_6$	0.02
$Fe^{48h}Cr_{22}C_6$	0.00
$Fe_{23}C_6$	1.91
$Fe_{23}B_6$	1.90

Table 3.6 The calculated total magnetization per unit cell.

IV. Conclusions

The thermodynamic and structural properties of Fe and B substituted $Cr_{23}C_6$ have been investigated using first-principles calculations based on the FLAPW method within GGA. The calculated equilibrium lattice parameter of $Cr_{23}C_6$ agrees well with published experimental data. Within the same computational scheme and model, Fe substituted structures and B substituted structures are calculated which do not have or insufficient.

The calculated formation enthalpies are -8.61 kJ mol^{-1}, -9.74 kJ mol^{-1} and -13.53 kJ mol^{-1} for $Cr_{23}C_6$, $Cr_{23}C_5B$ and $Cr_{23}B_6$, respectively. The calculated formation enthalpies at zero Kelvin show that boron stabilizes $M_{23}C_6$. By becoming more stable with boron substitution into $M_{23}C_6$, we can expect that the solubility of chromium in ferrite will decrease. There are experimental literatures concluding that boron containing steels have lower coarsening that non-boron containing steels.

The relation of increased stability of $M_{23}C_6$ by boron and reduced coarsening rate should be more studied. The implementation of calculated data into thermodynamic database such as MTDATA will be the next step which may give the explanation.

References

Abe, F., Proceedings of the Fourth International Conference on Recrystallization and Related Phenomena, Tsukuba, Japan, 289, 1999.

Albert, S. K., Kondo, M., Tabuchi, M., Yin, F., Sawada, K. and Abe, F., Improving the Creep Properties of 9Cr-3W-3Co-NbV Steels and their Weld Joints by the Addition of Boron, Metallurgical and Materials Transactions, 36A:333-343, 2005.

Bhadeshia, H. K. D. H., Design of Ferritic Creep-resistant Steels, ISIJ International, 41: 626-640, 2001.

Blügel, S. and Bihlmayer, G., Full-Potential Linearized Augmented Planewave Method, Computational nanoscience: Do It Yourself, 31:85, 2006.

Blum, R., Hald, J., Benidick, W., Rosselet, A. and Vaillant, J., Newly Developed High Temperature Ferritic-Martensitic Steels from USA, Japan and Europe, International VGB Conference – Fossil-fired Power Plant with Advanced Design Parameters, Kolding, Denmark, June, 1993.

Born, M., Quanum mechanics in impact processes, Z. Physik, 38:803, 1926.

Born, M. and Oppenheimer, R., Ann. Phys. (Leibzig), 84:457, 1930.

Bowman, A. L., Arnold, G. P., Storms, E. K. and Nereson, N. G., The crystal structure of $Cr_{23}C_6$, Acta Cryst, 28:3102, 1972.

Callister, W. D., Material Science and Engineering: An Introduction 7th Edition, Wiley, 2007.

Dieter, G. E., Mechanical Metallurgy SI Metric Edition, McGraw-Hill, London, 439, 1988.

Ennis, P. J. and Czyrska-Filemonowicz, A., Recent advances in creep-resistant steels for power plant applications, *Sādhanā*, 28: 709-730, 2003.

Freeman, A. J. and Wimmer, E., Annu. Rev. Mater. Sci., 25:7, 1995.

Guillermet, A. F. and Grimvall, G., J. Phys. Chem. Solids, 53:105, 1992.

Harvey, P. D., Engineering Properties of Steel, Am. Soc. Met. 1982.

Hedin, L. and Lundqvist, B. I., J. Phys. C: Solid St. Phys., 4:2062, 1971.

Hättestrand, M. and Andrén, H.-O., Boron distribution in 9 – 12% chromium steels, Materials Science and Engineering, 279:33-37, 1999.

Henriksson, K. O. E., Sandberg, N. and Wallenius, J., Carbides in stainless steels: Results from *ab initio* investigations, Applied Physics Letters, 93:191912, 2008.

Hofer, P., Miller, M. K., Babu, S. S., David, S. A. and Cerjak, H., Investigation of Boron Distribution in Martensitic 9% Cr Creep Resistant Steel, ISIJ International, 42:62-66, 2002

Hohenberg, P. and Kohn, W., Inhomogeneous Electron Gas, Physical Review B, 136:864, 1964.

Horiuchi, T., Igarashi, M. and Abe. F., Improved Utilization of Added B in 9Cr Heat-Resistant Steels Containing W, ISIJ International, 42:67-71, 2002.

Jiang, C., First-principles study of structural, elastic, and electronic properties of chromium carbides, Applied Physics Letters, 92:041909, 2008.

Jansen, H. J. F. and Freeman, A. J., Phys. Rev. B, 30:561, 1984.

Jiang, C., First-principles study of structural, elastic, and electronic properties of chromium carbides, Appl. Phys. Lett., 92:041909, 2008.

Jost, R. and Pais, A., Phys. Rev. 82:840, 1951.

Kleykamp, H., J. Alloys Compd., 321:138, 2001.

Kohn, W. and Sham, L. J., Self-Consistant Equations Including Exchange and Correlation Effects, Physical Review A, 140:1133-1138, 1965.

Kuo, K., Jernkontorets Ann., 137:149, 1953.

Lee, J. H., Shishidou, T. and Freeman, A. J., Physical Reveiw B, 66:23310, 2002.

Levy, M., Proc. Natl. Acad. Sci. (USA), 76:6062, 1979.

Lundin, L., Fällman, S. and Andrén, H.-O., Materials Science and Technology, 13:233, 1997.

Meinhardt, D. and Krisement, O., Arch. Eisenhuettenwes, 33:493, 1962.

Mimino, T., Creep Rupture Strength of 9Cr-1Mo-V-Nb-B Steel Developed for Boiler Applications, The Society of Materials Science, Japan, 28, 1978.

Monkhorst, H. J. and Pack, J. D., Physical Reveiw B, 13:5188, 1976.

Ohodnicki, P. R., Cates, N. C., Laughlin, D. E., McHenry, M. E. and Widom, M., *Ab initio* theorical study of magnetization and phase stability of the $(Fe,Co,Ni)_{23}B_6$ and $(Fe,Co,Ni)_{23}Zr_6$ structures of $Cr_{23}C_6$ and $Mn_{23}Th_6$ prototypes, Physical Review B, 78:144414, 2008.

Perdew, J. P., Burke, K. and Ernzerhof, M., Physical Reveiw Letter, 77:3865; *ibid.* 78:1396(E), 1996.

Race, J. M. and Bhadeshia, H. K. D. H., Precipitation sequences during carburization of Cr-Mo steel, Materials Science and Technology, 8:875, 1992.

Robson, J. D. and Bhadeshia, H. K. D. H., Modelling precipitation sequences in power plant steels, Materials Science and Technology, 13:631, 1997.

Samson, S., The Structure of Metals and Intermetallic Compounds Sept. 1, 1953-Aug. 31, Final Report, ONR Contract Nonr-220-33. (California Institutute of Technology, Pasadena), 1964.

Sandberg, N., Henriksson, K. O. E. and Wallenius, J., Carbon impurity dissolution and migration in bcc Fe-Cr: First-principles calculations, Physical Review B, 78:094110, 2008.

Santos, A. V., Comparative study between LMTO and FLAPW into the calculation of the electronic structure of carbide $Cr_{23}C_6$, Physica B, 387:136-142, 2007.

Schrödinger, E., Ann. Physik. 79, 361, 1926.

Seo, S-W., Song, Y. Y., Rahman, G., Kim, I. G., Weinert, M. and Freeman, A. J., A Convergence Test of the Full-potential Linearized Augmented Plane Wave (FLAPW) Method: Ferromagnetic Bulk BCC Fe, Journal of Magnetics, 14:137, 2009.

Singh, D. J., Planewaves, pseudopotentials and the LAPW method, Kluwer Academic, Boston, 1994.

Slater, J. C., Phys. Rev. 51:846, 1937.

Wachter, O. and Ennis, P. J., Ph.D. Thesis, Teshnische Hohschule, Aachen, Germany, p. 6-16, 1995.

Weinert, M., Wimmer, E. and Freeman, A. J., Physical Review B, 26:4571, 1982.

Westgren, A., Jernkontorets Ann., 117:501, 1933.

Wimmer, E., Krakauer, H., Weinert, M. and Freeman, A. J., Physical Review B, 24:6864, 1981.

Villars, P. and Calvert, L. D., Pearson's handbooks of crystallographic data for intermetallic phase, Metals Park (OH): ASM; 1991.

Vinet, P., Rose, J. H., Ferrante, J. and Smith, J. R., Universal features of the equation of state of solids, J. Phys.: Condens. Matter, 1:1941-1963, 1989.

Xie, J. Y., Chen, N. X., Teng, L. D. and Seetharaman, S., Atomistic study on the site preference and thermodynamic properties for $Cr_{23-x}Fe_xC_6$, Acta Materialia, 53:5305-5312, 2005.

Xie, J., Shen, J., Chen, N. and Seetharaman, S., Site preference and mechanical properties of $Cr_{23-x}T_xC_6$ and $Fe_{21}T_2C_6$ (T = Mo, W), Acta Materialia, 54:4653-4658, 2006.

Yakel, H. L., Atom Distributions in Tau-Carbide Phases: Fe and Cr Distributions in $(Cr_{23-x}Fe_x)C_6$ with x=0, $0{\cdot}7_4$, $4{\cdot}1_3$ and $7{\cdot}3_6$, Acta Cryst., 43:230, 1987.

Curriculum Vitae

Name: Song, You Young

E-mail: spirited@postech.ac.kr

Date of birth: 2nd June, 1983

Place of birth: Seoul, South Korea

Education

M. S. 2010, POSTECH (Pohang, Korea), Graduate Institute of Ferrous Technology, Computational Metallurgy Group

B. S. 2008, POSTECH (Pohang, Korea), Department of Computer Science and Engineering / Department of Mathmatics